International Journal of Electrochemical Science 20 (2025) 100967

Contents lists available at ScienceDirect

International Journal of Electrochemical Science

journal homepage: www.sciencedirect.com/journal/international-journal-of-electrochemical-science

The influence of H_2S on the microstructure of API 5 L X65 pipeline steel: An electrochemical approach

Duberney Hincapié-Ladino [a], José Wilmar Calderón-Hernández [b,*], João Victor de S. Araujo [c], Rodrigo Magnabosco [d], Neusa Alonso-Falleiros [a]

[a] Department of Metallurgical and Materials Engineering, Escola Politécnica, University of São Paulo, Av. Prof. Mello Moraes, 2463, São Paulo, SP 05508-030, Brazil
[b] Grupo de Investigación Ingeniar, Facultad de Ciencias Básicas e Ingenierias, Corporación Universitaria Remington, Calle 51 #51-27, Medellín, Colombia
[c] Centro de Ciência e Tecnologia de Materiais, Instituto de Pesquisas Energéticas e Nucleares, Universidade de São Paulo, Brazil
[d] FEI, Mechanical Engineering Department, São Bernardo do Campo, São Paulo, Brazil

ARTICLE INFO

Keywords:
High strength low alloy steel
Potentiodynamic polarization
Hydrogen sulfide
Simulated pipeline environments

ABSTRACT

Pipelines and equipment made from microalloyed steels used in oil and gas production are exposed to aggressive environments: marine water on the exterior and hydrogen sulfide (H_2S)-rich environments inside. This study evaluated the corrosion behavior of two microalloyed steels (API 5 L X65) in solutions simulating internal and external pipeline conditions based on the NACE TM0284–11 standard. Potentiodynamic polarization was used to measure corrosion rates, and Scanning Electron Microscopy (SEM) with energy-dispersive X-ray Spectroscopy (EDS) characterized the microstructure and corrosion products. The results showed that solution B led to lower corrosion rates due to iron sulfide phase formation, while the steel without segregation bands exhibited superior performance in both solutions. Corrosion mechanisms were discussed based on experimental findings, thermodynamics, and kinetics.

1. Introduction

Microalloyed or high-strength low alloy steels (HSLA) are widely used in large-diameter pipes for oil and natural gas pipelines and tanks due to their excellent mechanical properties and weldability. Nevertheless, these materials are susceptible to both uniform and localized corrosion, which can lead to premature failures. Commonly, pipelines used for gas transport are produced in API X65, X70, and X80 grades [1]. Internally, these pipes are frequently exposed to highly corrosive aqueous environments, mainly containing hydrogen sulfide (H_2S) and carbon dioxide (CO_2), typical components of oil and gas reserves.

Steel corrosion in aqueous environments with H_2S occurs through two primary reactions: the anodic dissolution of the metal and the cathodic reduction of one or more species in the electrolyte. Hydrogen sulfide can accelerate or inhibit steel corrosion, depending on several factors. For iron [2] and microalloyed steels [3] in acidic electrolytes, the corrosion rate typically increases with the addition of H_2S. Conversely, corrosion may be inhibited by the formation of protective iron sulfides (FexSy) or other metastable phases [4,5], whose structure and properties depend on variables such as H_2S concentration, temperature, pH, and immersion time [5].

At least eight different iron sulfides have been identified in H_2S/steel systems [5], many of which are nonstoichiometric and vary in crystallinity despite having similar chemical formulas. The corrosion protection offered by iron sulfides decreases in the order of mackinawite, pyrrhotite, and pyrite [5,6]. For example, Vedage [4] observed pyrrhotite as the primary corrosion product in 4130 steels exposed to H_2S-saturated electrolytes with 3 % NaCl at 22–95 °C temperatures.

The addition of alloying elements in steel can also influence corrosion behavior. For example, phosphorus is one of the most harmful impurities in HSLA steels. Studies have shown that increasing phosphorus content in steel raises the corrosion rate in NACE solutions with H_2S additions [7,8]. Similarly, Cleary and Greene [9] reported that phosphorus and carbon significantly increase corrosion rates, while copper additions have negligible effects in acidic environments [9,10].

Steels recommended for oil and gas pipelines where H2S is present are known as sour-service steels. To achieve the desired properties in these materials, it is necessary to add microalloying elements and perform thermomechanical treatments that modify the microstructure and, consequently, the corrosion resistance. For example, it has been

---

* Corresponding author.
E-mail address: jose.calderon01@uniremington.edu.co (J.W. Calderón-Hernández).

https://doi.org/10.1016/j.ijoes.2025.100967
Received 13 December 2024; Received in revised form 27 January 2025; Accepted 6 February 2025

reported that the presence of pearlite within ferrite grains can increase corrosion susceptibility in this case due to a galvanic mechanism [11, 12]. Sharma and Chhibber [13] used different thermal treatment routes to obtain samples of several microstructures in X70 steel. These authors reported that polygonal ferrite and fine-grained ferrite microstructures inhibit the corrosion rate compared to the tempered martensitic microstructure. Huang et al. [14] found higher polarization resistance in microalloyed steels with a greater proportion of ferrite in the Widmanstätten morphology and Lucio-Garcia [15] report that martensite content strongly influences corrosion rates in microalloyed steels.

Although material selection standards guide the choice of materials for specific applications, they often lack detailed information on the microstructural, physical, or electrochemical phenomena affecting these recommendations. This study compares the corrosion resistance of two API 5 L X65 pipeline steels with different microstructures. Polarization resistance tests were conducted in two electrolytes, Solution A and Solution B (NACE solutions) [16], with H_2S injection. Finally, a mechanism is proposed to explain the observed corrosion behavior.

2. Experimental procedure

Two commercial API 5 L X65 pipeline steels, designated X65A and X65B, were used in this study. Their chemical compositions are provided in Table 1.

Samples for electrochemical testing and microstructural characterization were cut and mounted in resin, exposing an area of 1 cm^2 perpendicular to the rolling direction through the material thickness.

For microstructural characterization, the samples were initially ground with 1200-grit silicon carbide paper, then polished with diamond suspensions of 6 μm, 3 μm, and 1 μm. The polished samples were etched with a 2 % nitric acid solution in alcohol (Nital) to reveal the microstructures, which were subsequently analyzed using scanning electron microscopy (SEM).

For polarization resistance (Rp) tests, the samples were ground with silicon carbide paper to #600 grit, thoroughly washed with ethanol, and dried using hot air. The electrolytic solutions used in the experiments, referred to as Solution A and Solution B, were prepared in accordance with the NACE TM0284–2011 standard. Solution A consisted of 5.0 wt% NaCl and 0.5 wt% CH_3COOH dissolved in distilled water, while Solution B represented Substituted Ocean Water. Both solutions were initially deaerated with nitrogen gas for one hour before use. Subsequently, the solutions were transferred to a 700 mL electrochemical cell and deaerated again with nitrogen for another thirty minutes. Following this, hydrogen sulfide (H_2S) gas was bubbled into the test solutions at a rate of 200 mL/min for one hour, reducing the pH of Solution A to 2.7 and Solution B to 4.7.

The polarization resistance measurements were performed using an EG&G Princeton Applied Research 273 A potentiostat connected to a computer. A conventional three-electrode test cell was employed, consisting of a platinum wire as the counter electrode, a saturated calomel electrode (SCE) as the reference electrode, and the X65 steel samples as the working electrode. The measurements were carried out by scanning the potential from a cathodic overpotential of −10 mV to an anodic overpotential of + 10 mV relative to the open-circuit potential at a scan rate of 1 mV/s. The linear polarization resistance (LPR) was determined from the slope of the overpotential versus current density curves. Rp measurements were recorded every 10 min over one hour, and at least three independent tests were conducted for each steel sample under ambient conditions (25 ± 3 °C).

The corrosion products and microstructures were analyzed using SEM and energy-dispersive X-ray spectroscopy (EDS) (Obducat CamScan model CS3200LV). Additionally, grazing incidence X-ray diffraction (GI-XRD) was performed to characterize the corrosion products formed on the samples immersed in Solution B for 2 and 24 h. Diffraction was carried out using Cu Kα radiation at an incidence angle of 10°, with a 2θ range of 5°–100° and a scan rate of 1°/min.

3. Result and analysis

3.1. Microstructural analyses

Two types of API 5 L X65 steels with microstructural differences were selected for this investigation. The steels were designed as X65A and X65B, and their microstructures are presented in Figs. 1 and 2, respectively. The microstructure of X65A consists of refined ferrite grains (F), acicular ferrite (AF), and martensite/austenite (M/A) microconstituents, which are homogeneously distributed throughout the matrix (Fig. 1.a). Additionally, X65A shows a lower density of inclusions (Fig. 1.b). In contrast, the microstructure of X65B comprises ferritic grains (F) and pearlite bands (PB) aligned with the rolling direction (Fig. 2.a), exhibiting a higher density of inclusions compared to X65A (Fig. 2.b). For both steels, elongated Mn inclusions were not observed.

3.2. Polarization resistance technique

Figs. 3 and 4 present the Polarization Resistance (Rp) values as a function of immersion time for solutions A and B.

An average Rp value was calculated from the data obtained in three tests. Fig. 5 compares the average Rp values for solutions A and B. The analysis indicates that X65B steel is more susceptible to corrosion than X65A steel in both solutions. Furthermore, the Rp results demonstrate that solution A is more aggressive than solution B, as evidenced by the lower Rp values for both steels in solution A.

Table 2 presents the average Rp values and the E_{corr} intervals for each steel-electrolyte system during the Rp acquisition.

As observed in Table 2, although the E_{corr} values were relatively stable for X65A steel (ranging from −680 to −665 mV$_{SCE}$ in solution A and from −780 to −753 mV$_{SCE}$ in solution B), the Rp results for this steel showed greater variation compared to X65B. Despite these related parameters, they represent different phenomena: E_{corr} indicates where cathodic and anodic reactions are balanced, whereas Rp measures how difficult it is for electrochemical reactions (such as oxidation and reduction) to occur at the surface of metals. Therefore, the variability in Rp is attributed to the inherent microscopic randomness and heterogeneity in electrochemical systems, which can lead to stochastic, probabilistic, and fluctuating behavior. Notwithstanding, Fig. 5 shows that the tendency of Rp presented by X65A steel in solution B was higher.

Fig. 6 illustrates the corrosion morphology observed after polarization resistance (Rp) tests in solution A. Both uniform and localized corrosion were identified, with localized corrosion associated with non-metallic inclusions. EDS analysis of the surface for both steels revealed similar spectra; therefore, the analysis focused on regions of localized corrosion caused by the dissolution of inclusions. It can be considered that the EDS technique is not sensible to low-concentration elements (generally below 1 w%); the spectrum shown in Fig. 6 presents indexed Fe peaks and maybe Mn (both steels contain approximately 1.5 w% according to Table 1), although these peaks overlap.

Fig. 7 depicts the corrosion morphology observed after both steels'

Table 1
Chemical compositions of the API 5 L X65 pipeline steels (values in wt%).

Sample	C	Mn	P	S	Si	Cu	Al	Cr	Ni	V+Ti+Nb
X65A	0.04	1.52	0.005	0.001	0.33	0.013	0.035	0.16	0.012	0.057
X65B	0.07	1.52	0.021	0.003	0.21	0.010	0.043	0.02	0.19	0.103

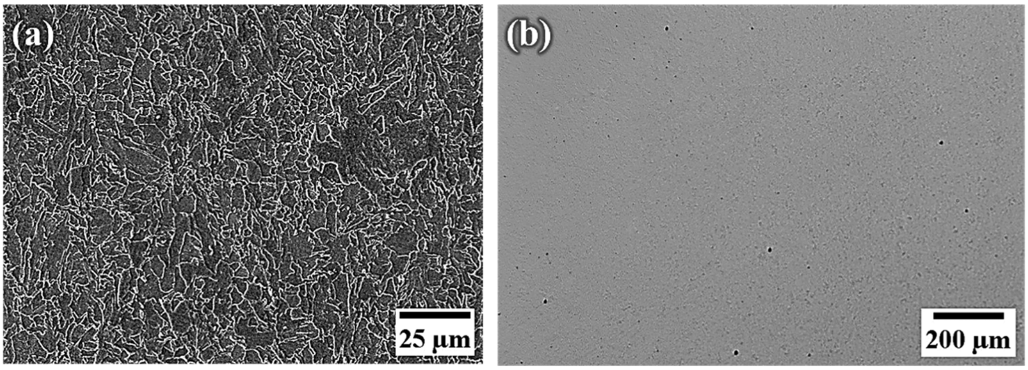

Fig. 1. (a) Scanning micrograph showing the microstructure of X65A steel, with acicular ferrite and Martensite/Austenite (M/A) microconstituents on a polished surface etched with 2 % Nital. The image was obtained using the secondary electron (SE) mode at an acceleration voltage of 15 kV. (b) Optical microscopy image of the polished surface illustrating the inclusion distribution (Level D1) as per ASTM E45.

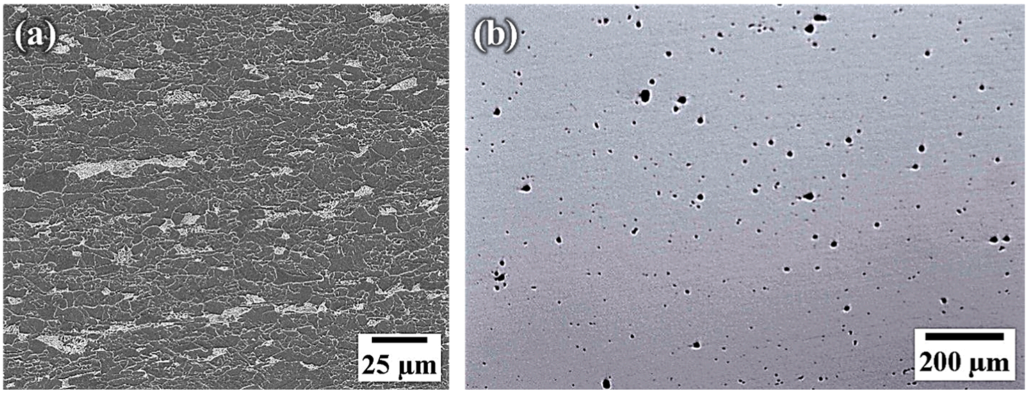

Fig. 2. (a) Scanning micrograph showing the microstructure of X65B steel, with ferritic grains and pearlite bands on a polished surface etched with 2 % Nital. The image was obtained using the secondary electron (SE) mode at an acceleration voltage of 15 kV. (b) Optical microscopy image of the polished surface illustrating the inclusion distribution (Level D4) as per ASTM E45.

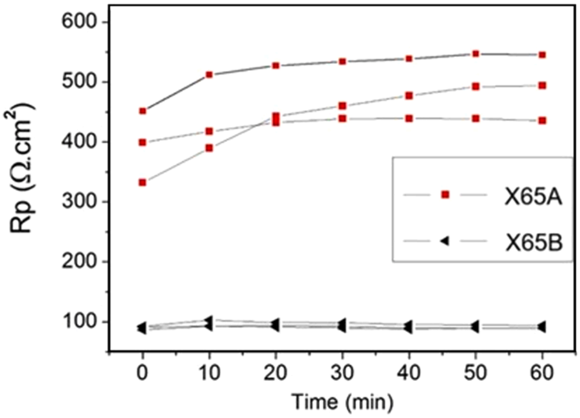

Fig. 3. Polarization resistance (Rp) of steel samples measured in NACE Solution A after H_2S injections, prepared according to the NACE TM0284–2011 standard.

Rp tests in solution B. Following the tests, a black product was observed on the sample surfaces. SEM and EDS analysis confirmed the presence of a uniform FeS layer in both steels in solution B.

3.3. X-ray diffraction (XRD)

Figs. 6 and 7 present the microstructural analysis of surfaces exposed to solutions A and B, respectively. The surfaces corroded by solution A did not form corrosion products due to the high aggressiveness of the solution. In contrast, corrosion products were observed only in samples immersed in solution B.

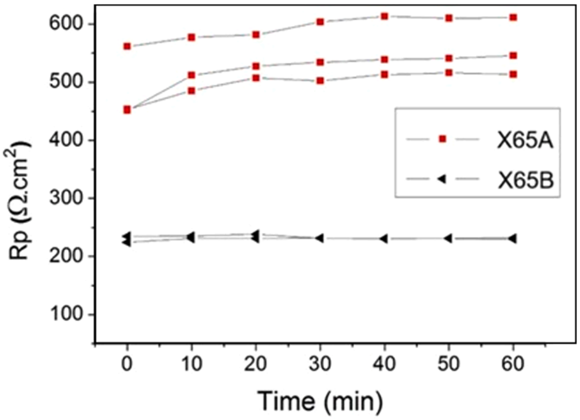

Fig. 4. Polarization resistance (Rp) of steel samples measured in NACE Solution B after H_2S injections, prepared according to the NACE TM0284–2011 standard.

Solution B generated similar corrosion products in both steels. To characterize these products, immersion tests in solution B were conducted for 2 and 24 h on X65A steel (selected as the more technological and interesting steel), followed by analysis using Grazing Incidence X-ray Diffraction (GI-XRD). Fig. 8 shows the resulting diffractograms. Only ferrite was detected after 2 h of immersion, indicating that this immersion time was insufficient to produce corrosion products detectable

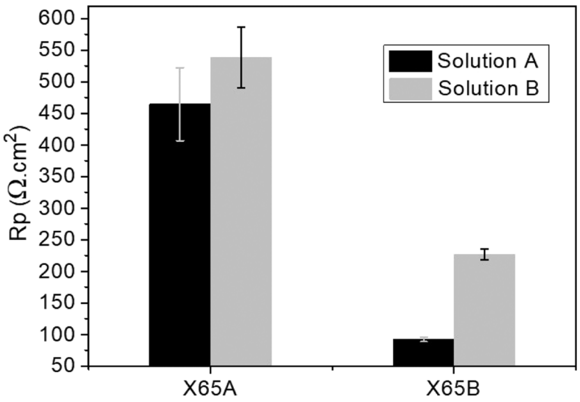

Fig. 5. Comparison of average polarization resistance (Rp) values for both solutions (NACE Solution A and B) and the different steel samples (X65A and X65B).

Table 2
Average polarization resistance (Rp) values and corresponding E_{corr} intervals measured during Rp acquisition for each sample.

SOLUTION	SAMPLE	Rp (Ω. cm^2)	E_{corr} (mV SCE)	E_{corr} (mV EH)	Characteristic E_{corr} (mV EH)
A	X65A	464 ± 58	−680 to −665	−438 to −423	−438 to −423
	X65B	92 ± 40	−680 to −666	−438 to −424	
B	X65A	538 ± 48	−780 to −753	−538 to −511	−538 to −508
	X65B	226± 9	−769 to −750	−527 to −508	

by XRD, while the sample immersed for 24 h revealed the presence of ferrite and mackinawite, which is a typical Fe-S compound.

4. Discussion

The chemical composition's influence on the steel's corrosion resistance was initially analyzed. Adding Cu, Cr, and Ni has been reported to enhance the corrosion resistance of pipeline steels [7]. Specifically, Cu additions are significant only at pH above 4.5, as they promote the stable FeS film [17]. Moreover, incorporating Cr and Ni reduces the corrosion rate and, consequently, hydrogen absorption, with this effect primarily attributed to Cr [17,18].

Conversely, the presence of phosphorus (P) and carbon (C) adversely affects corrosion resistance [19,20]. In the present study, no correlation was observed between the amounts of Cu and Ni and the corrosion resistance of the steels (as shown in Table 1 and Figs. 3 and 4). Thus, the effect of Cu is not considered significant under the studied conditions. However, the Cr content positively correlated with the polarization resistance (Rp) of steel X65A in both solutions. In contrast, detrimental elements such as P and C exhibited an inverse trend, where higher concentrations reduced Rp values.

These results, however, do not account for the potential effects of microstructure and non-metallic inclusions. The literature [11,12] suggests that pearlite reduces the corrosion resistance of microalloyed steels in H_2S-saturated solutions via a galvanic effect. This occurs because pearlite islands, rich in carbon, are nobler than the ferrite matrix. Additionally, a high density of non-metallic inclusions increases the corrosion rate because their chemical composition is less noble than the steel matrix.

The findings of this study align with previous research: elevated levels of P and C result in segregation and the formation of pearlite bands, which increase the corrosion rate. Similarly, a higher density of non-metallic inclusions exacerbates the corrosion process.

The homogeneous ferrite matrix in X65A significantly enhances corrosion resistance by mitigating the effects of inhomogeneities, such as inclusions. Surface inhomogeneities in metallic materials affect the spatial distribution and dimensions of anodic and cathodic domains, which are critical for the occurrence of corrosion reactions. A range of crystallographic and physical characteristics influence these domains, including lattice distortions, grain boundary configurations, and interfaces between inclusions and the matrix. These microscopic irregularities serve as active sites for electrochemical processes, facilitating mechanisms such as metal dissolution and localized corrosion phenomena. [21]. In addition, the interface between the inclusion and the matrix behaves as a micro-crevice, serving as a preferential site for corrosion initiation [22,23]. In X65A, the homogeneous ferrite matrix with a low density of inclusions decreases the number of active sites for corrosion, contributing to superior performance in both solutions.

Pourbaix and Evans diagrams were constructed to investigate the growth of the iron sulfide layer and the corrosion rate in both solutions further. The Pourbaix diagram was based on equilibrium equations for the Fe-H_2O-S system [20], as outlined in Equations 1–5. Electrode potentials ranging from −1–0 V (EH), pH values from 0 to 10, and a temperature of 25°C were employed. Fig. 9 presents the Fe-S-H_2O diagram, which includes the pH values for solutions A and B (pH 3.0 and 5.0, respectively) and the average E_{corr} values (E_A and E_B).

(1) Reaction H^+/H_2: $2\,H^+ + 2e = H_2$

$E_{H+/H2}$= -0.059 pH

(2) Reaction Fe^{+2}/Fe: $Fe^{+2} + 2e = Fe$

$E_{Fe+2/Fe} = -0.409 + 0.0295.\log(Fe^{+2})$

(3) Reaction FeS/Fe: $FeS + 2\,H^+ + 2e- = Fe + H_2S$

$E_{FeS/Fe} = -0.376 - 0.059\ pH - 0.0296.\log(H_2S_{aq})$

(4) Reaction FeS_2/FeS: $FeS_2 + 2\,H^+ + 2e- = FeS + H_2S$

$E_{FeS2/FeS} = -0.165 - 0.059\ pH - 0.0296.\log(H_2S_{aq})$

(5) Reaction FeS_2/H_2S: $FeS_2 + 4\,H^+ + 2e^- = Fe^{+2} + 2\,H_2S$

$E_{FeS2/H2S} = -0.133 - 0.118\ pH - 0.0296.\log\ [(Fe^{+2})(H_2S_{aq})]$

Table 3 presents the equilibrium potentials obtained from the equilibrium reactions in the pH of the solutions studied and experimental E_{corr} values. The activity coefficient of H_2Saq was assumed to be unity [21–24]. Based on the equilibrium electrode potentials listed in Table 3 and using the Butler-Volmer equation to describe the electrochemical kinetics and establish the relationship between current density and polarization, schematic polarization curves (Evans diagrams) were constructed for the electrode reactions of each system. (iron immersed in solutions A and B), as shown in Figs. 10 and 12.

The Rp values, displayed in Fig. 4, indicate that for both steels, Rp is lower in solution A than in solution B. These findings are further analyzed using the polarization curves of the electrode reactions in each system, as discussed below.

Fig. 10 illustrates the partial reactions for the hydrogen electrode, the FeS_2/H_2 S reaction, and the iron electrode. A Tafel slope of 118 mV [22–25] and an exchange current density of 10 −6 A·cm−2 [23–26] were used for the hydrogen cathodic reaction. For the iron anodic

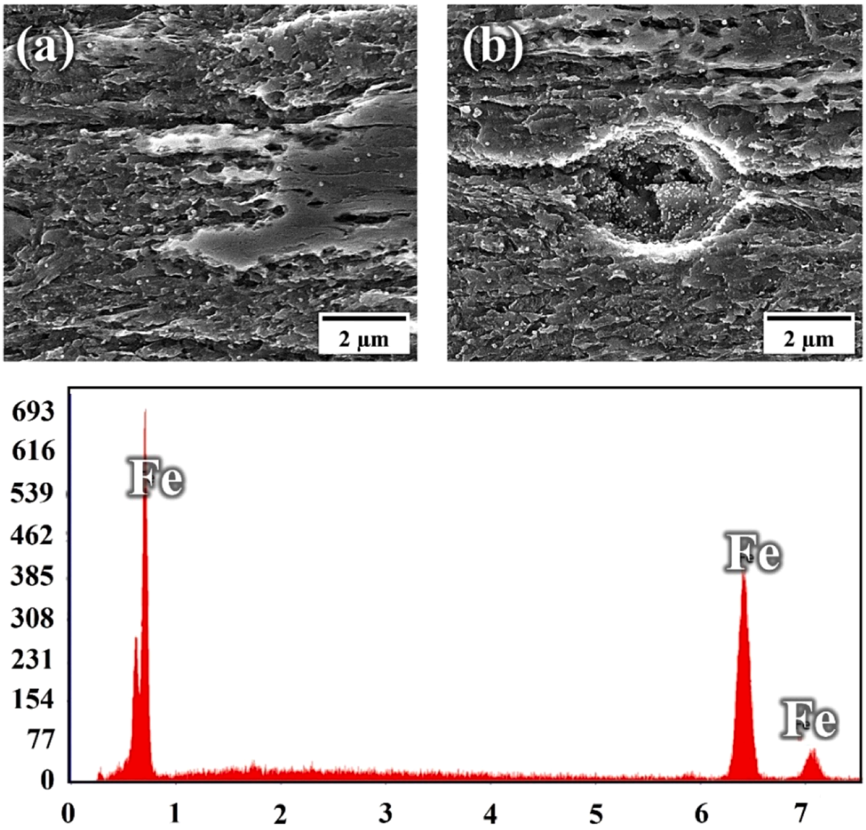

Fig. 6. Scanning electron micrographs (SEM) and EDS analysis after Rp tests in Solution A. (a) X65A steel, (b) X65B steel, and (c) EDS spectrum of the localized corrosion region. The SEM images were obtained in BSE mode at an acceleration voltage of 15 kV.

reaction, a Tafel slope of 60 mV and an exchange current density of 10^{-7} A·cm^{-2} were applied [24–27]. Additionally, a Tafel slope of 80 mV and an exchange current density of 5×10^{-7} A·cm^{-2} were used for the FeS_2/H_2S reaction.

It is important to note that the current density values were estimated based on the aforementioned considerations.

The reactions governing the kinetics of the mixed electrode in solution A are the cathodic hydrogen reaction, the cathodic FeS_2 /H_2 S reaction, and the anodic iron reaction. The intersection of the combined cathodic reactions (hydrogen and FeS2/H2 S) and the anodic iron reaction determined the corrosion potential. The results in Fig. 11 indicate that the experimental corrosion potential (E_{corr}A) for solution A, ranging from −438 to −418 mV (EH), shows a good correlation with the experimental data.

The same procedure was applied to solution B, and the results are shown in Fig. 12. The equilibrium potentials for solution B are lower than those observed for solution A (as indicated in Table 3). In the specific case of the hydrogen reaction, the higher pH of solution B compared to solution A decreases the equilibrium potential and the exchange current density [28].

At pH 5, the exchange current density of hydrogen reaches 10^{-7}A. cm^{-2}; thus, the cathodic curve of hydrogen moves for lower potentials and current densities.

Another important fact is that the iron curve does not modify its position; therefore, after the displacement of the other reactions, the iron anodic curve became nobler than the partial anodic reaction FeS/Fe. Fig. 13 shows the sum of the cathodic and anodic curves, and it can be observed that the experimental corrosion potential is in the expected interval (E_{corr}B).

Figs. 11 to 13 aim to analyze the corrosion mechanisms of iron samples immersed in solutions A and B. The experimental results indicate that solution A is more corrosive than solution B, as evidenced in Fig. 5.

Fig. 14 demonstrates that solution A exhibits higher Ecorr and icorr values than solution B. Additionally, in Figs. 10 and 12, the position of the hydrogen cathodic polarization curve shifts to lower potentials in solution B, reflecting the influence of the pH difference between the two solutions. This lower equilibrium potential of the hydrogen cathodic curve in solution B contributes to a reduced corrosion rate.

As previously discussed, corrosion products were observed only on samples immersed in solution B. This finding aligns with reports from other authors [25–29], who observed the absence of corrosion products in SAE 1018 steel when immersed in acetic acid solutions containing chloride and H_2S. Ma et al. [5] have further highlighted the limited formation of iron sulfides at low pH values due to the higher solubility of these phases. Iron sulfides only become stable at pH > 3, whereas between pH 3 and 5, corrosion products primarily consist of mackinawite and troilite.

Samples immersed in solution B generated a greater amount of corrosion products. The improved corrosion resistance of the steels in this solution can be attributed to the formation of a protective FeS layer, as suggested in the literature [12–30]. However, Figs. 12 and 13 propose an alternative mechanism that explains the higher amount of corrosion products in solution B and its relationship with the lower corrosion rate, independent of the protective properties of the FeS film.

Fig. 10 illustrates the partial reactions of iron immersed in solution A saturated with H_2S. The cathodic hydrogen and anodic iron reactions primarily define the corrosion current density in this environment. An additional reaction influencing the corrosion rate is the cathodic FeS $_2$/H_2 S reaction, which stabilizes H_2S and facilitates the hydrogen evolution reaction (HER). As a result, the growth of iron sulfides in solution A is minimal. This analysis suggests that microalloyed steel immersed in solution A does not produce a stable FeS layer on its surface. Instead, iron dissolution occurs at a higher rate, stabilizing H_2 S and promoting

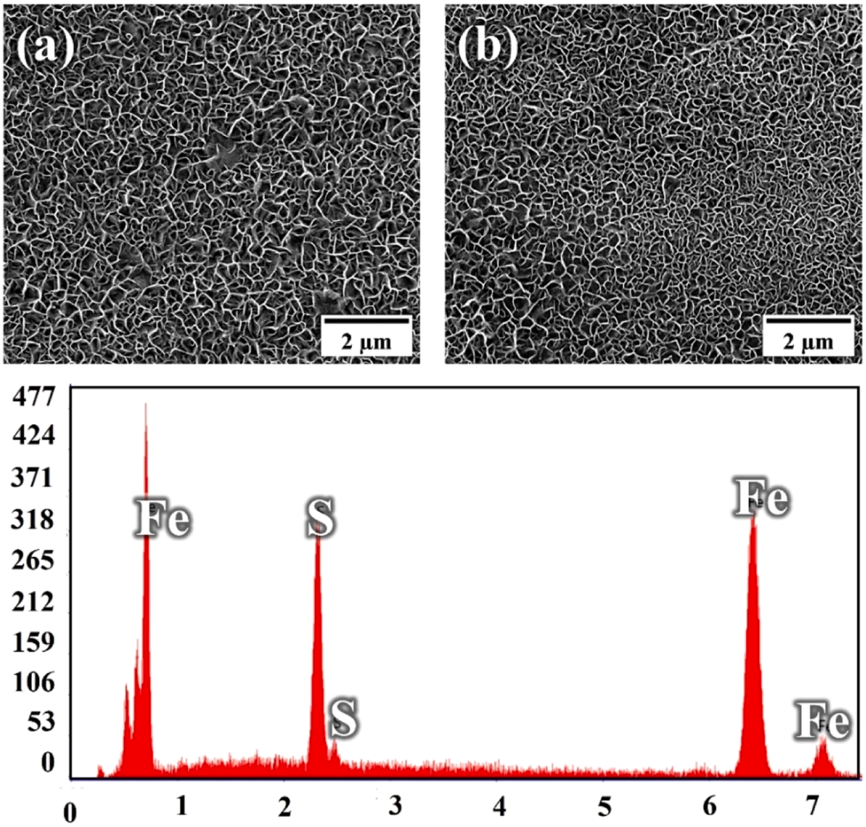

Fig. 7. Scanning electron micrographs (SEM) and EDS analysis after Rp tests in Solution B. (a) API 5 L X65A steel, (b) API 5 L X65B steel, and (c) EDS spectrum of the surface of API 5 L X65B steel. The SEM images were obtained in BSE mode at an acceleration voltage of 15 kV.

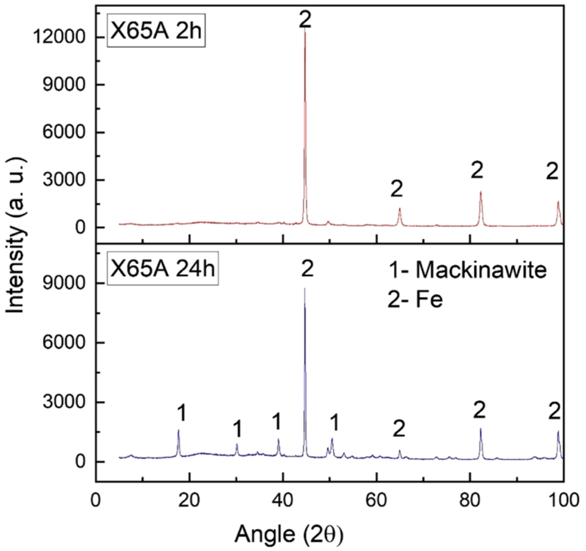

Fig. 8. Grazing Incidence XRD (GI-XRD) patterns of corrosion products generated by solution B.

hydrogen adsorption and entry into the steel.

For solution B, the corrosion rate of the steel is defined by the partial reactions shown in Fig. 12. The anodic FeS/Fe reaction and the cathodic FeS_2 /FeS reaction contribute to FeS formation. In contrast, the reaction involving the cathodic hydrogen reaction and the anodic iron reaction occurs at significantly lower current densities.

This comparison demonstrates that steel corrosion in solution B results in a higher amount of FeS while exhibiting a lower iron dissolution

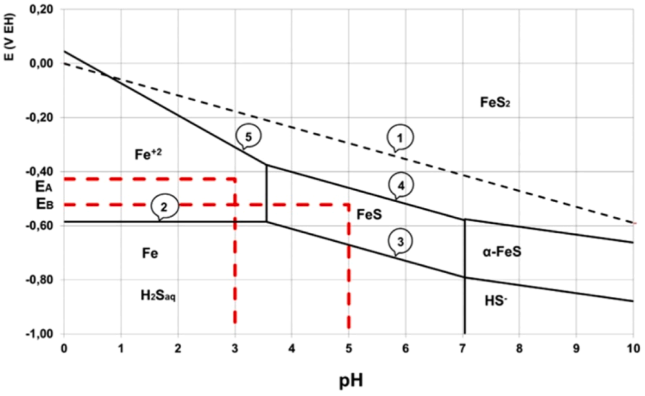

Fig. 9. Detailed Pourbaix diagram for the Fe-H2O-S system, illustrating the Ecorr values for solutions A and B. The dashed line represents the equilibrium reaction of hydrogen.

Table 3
Equilibrium and experimental corrosion potentials.

Parameter	Potential (mV EH)	
	Solution A	Solution B
E_{corr}	−438 to −418	−538 to −508
$E_{H+/H2}$	−177	−295
$E_{Fe+2/Fe}$	−586	−586
$E_{FeS/Fe}$	-	−671
$E_{FeS2/FeS}$	-	−460
$E_{Fe+2/FeS}$	−309	-

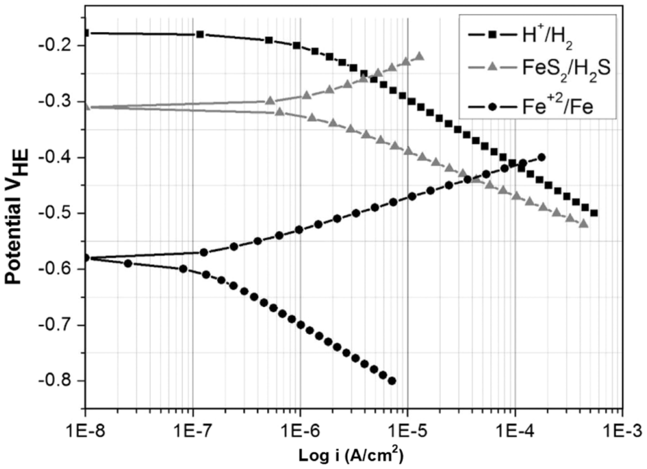

Fig. 10. Potentiodynamic polarization curves for Fe system reactions in solution A.

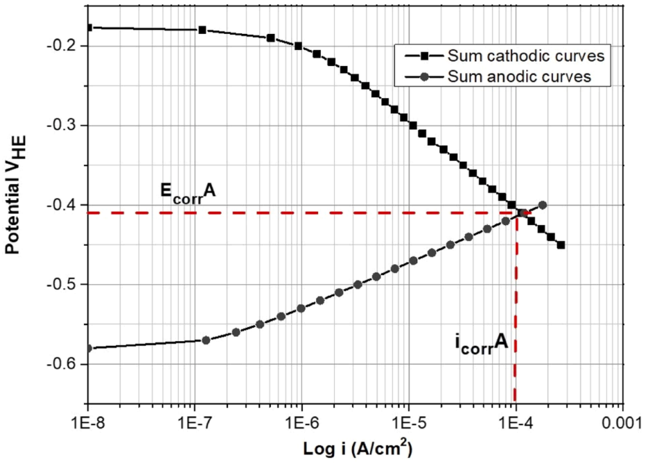

Fig. 11. Anodic and cathodic potentiodynamic polarization curves of Fe system in solution A. The average of potential (E_{corr}A) and current density (i_{corr}A) are indicated.

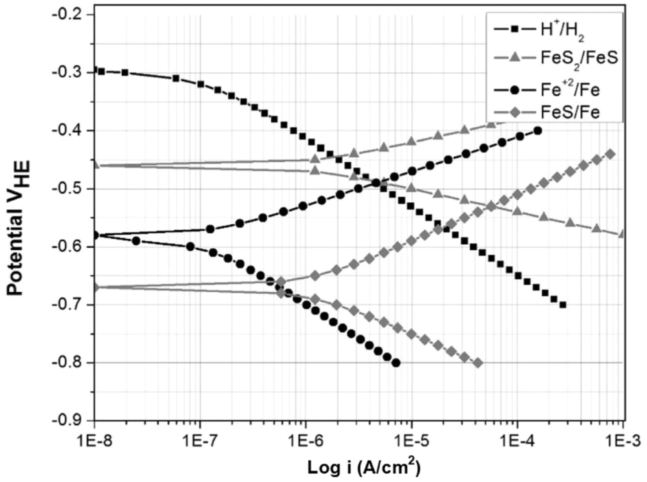

Fig. 12. Potentiodynamic curves for Fe system reactions in solution B.

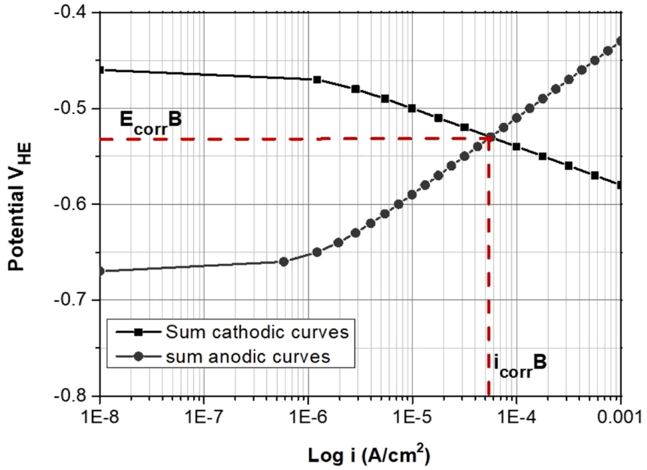

Fig. 13. Anodic and cathodic potentiodynamic polarization curves of Fe system in solution B. The average of potential (E_{corr}B) and current density (i_{corr}B) are indicated.

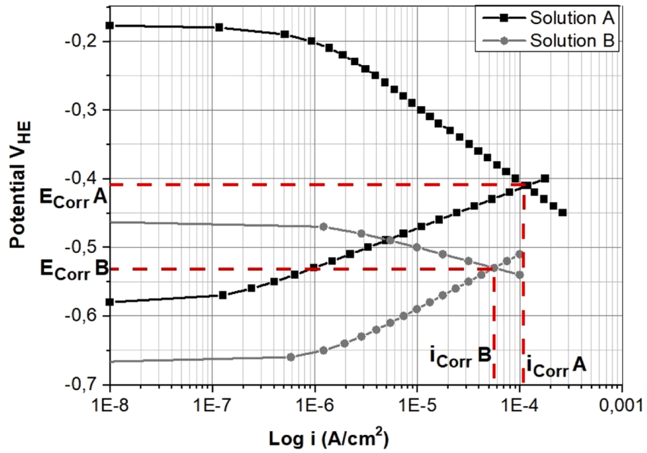

Fig. 14. Comparison between potentiodynamic polarization curves of solutions A and B.

rate than in solution A. It is important to emphasize that these findings do not dismiss the protective role of the FeS film. Regardless of its formation, the lower dissolution rate of the steel in solution B can be attributed to the higher pH. Moreover, the increased amount of corrosion products in solution B further reduces the dissolution rate of iron.

5. Conclusion

a) The corrosion rate of HSLA steel in H_2S-rich solutions is influenced by the electrolyte's aggressiveness and the steel's microstructural characteristics, which play a significant role in its electrochemical behavior.
b) The corrosion rates and potentials of microalloyed steels in NACE solutions can be interpreted through theoretical predictions of polarization curves (Tafel) for reactions involving Fe, H_2, FeS_2, FeS, and H_2S.
c) Experimental corrosion potentials align with theoretical predictions, explaining the measured polarization resistance and the amount of corrosion products formed on the steel's surface. This indicates that the main corrosion product is FeS, which clarifies why the corrosion rate is largely unaffected by the protective properties of these products.

d) Although both steels form FeS in Solution B, differences in corrosion resistance were observed. X65A demonstrated superior resistance due to its homogeneous ferrite matrix (lacking pearlite) and a lower density of inclusions.

CRediT authorship contribution statement

Hincapié-Ladino Duberney: Writing – original draft, Investigation. **Alonso-Falleiros Neusa:** Writing – review & editing, Writing – original draft, Supervision, Methodology. **Magnabosco Rodrigo:** Writing – review & editing, Writing – original draft, Methodology. **Araujo João Victor de S.:** Writing – review & editing. **Calderón-Hernández José Wilmar:** Writing – original draft, Investigation.

Declaration of Competing Interest

The authors declare that they have no known competing financial interests or personal relationships that could have appeared to influence the work reported in this paper.

Acknowledges

We want to thank the National Council for Scientific and Technological Development (CNPq), the University of São Paulo (Brazil), and Remington University Corporation (Colombia) for their financial support.

References

[1] J.Y. Koo, M.J. Luton, N.V. Bangaru, R.A. Petkovic, D.P. Fairchild, C.W. Petersen, Metallurgical design of ultra-high strength steels for gas pipelines, Int. Offshore Polar Eng. Conf. 5 (2003) 10–18.
[2] H. Ma, X. Cheng, S. Chen, C. Wang, J. Zhang, An AC impedance study of the anodic dissolution of iron in sulfuric acid solutions containing hydrogen sulfide, J. Electroanal. Chem. 451 (1998) 11–17.
[3] S. Arzola, J. Genesca, The effect of H2S concentration on the corrosion behavior of API 5L X70 steel, J. Solid State Electrochem. (2005) 197–200.
[4] H. Vedage, T.A. Ramanarayanan, J.D. Mumford, S.N. Smith, Electrochemical growth of iron sulfide films in H2S-saturated chloride media, Corrosion 49 (1993) 114–121.
[5] H. Ma, X. Cheng, G. Li, S. Chen, The influence of hydrogen sulfide on corrosion of iron under different conditions, Corros. Sci. 42 (2000) 1669–1683.
[6] A.G. Wikjord, T.E. Rummery, F.E. Doern, D.G. Owen, Corrosion and deposition during the exposure of carbon steel to hydrogen sulfide-water solutions, Corros. Sci. 20 (1980) 651–671.
[7] A.C. Palmer, R.A. King. Subsea Pipeline Engineering, First ed., PennWell Corporation, USA, 2004, p. 570.
[8] E.M. Riecke, B. Johnen, R. Moeller, The effect of phosphorus on hydrogen uptake by iron in acid sulfate and sulfide solutions, Corrosion 27 (1987) 1027–1039.
[9] H.J. Cleary, N.D. Greene, Corrosion properties of iron and steel, Corros. Sci. 7 (1967) 821–831.
[10] M. Stratmann, K. Bohnenkamp, T. Ramchandra, The influence of copper upon the atmospheric corrosion of iron, Corros. Sci. 27 (1987) 905–926.
[11] (nueva]) L.R. Jacobo, R. García-Hernández, V.H. López-Morelos, et al., Effect of acicular ferrite and bainite in API X70 steel obtained after applying a heat treatment on corrosion and cracking behaviour, Met. Mater. Int. 27 (2021) 3750–3764, https://doi.org/10.1007/s12540-020-00805-7.
[12] J.D. Santos Martinez, D.H. Ladino, J.W. Calderón Hernández, N.A. Falleiros, H. G. de Melo, Corrosion characterization of new low manganese microalloyed X65 steels in sour and non-sour synthetic seawater, J. Mater. Res. Technol. 18 (2022) 3198–3214.
[13] Lochan Sharma, Rahul Chhibber, Microstructure evolution and electrochemical corrosion behaviour of API X70 linepipe steel in different environments, Int. J. Press. Vessels Pip. 171 (2019) 51–59, https://doi.org/10.1016/j.ijpvp.2019.01.013.
[14] H. Huang, W. Tsai, J. Lee, Electrochemical behavior of the simulated heat-affected zone of A516 carbon steel in H_2S, Electrochim. Acta 41 (1996) 1191–1199.
[15] M.A. Lucio-Garcia, J.G. Gonzalez-Rodriguez, M. Casales, L. Martinez, J.G. Chacon-Nava, M.A. Neri-Flores, Effect of heat treatment on H2S corrosion of a micro-alloyed C–Mn steel, Corros. Sci. 51 (2009) 2380–2386.
[16] NACE Standard TM0284-2003, Evaluation of pipeline and pressure vessel steels for resistance to hydrogen-induced cracking, Houston, TX: NACE, 2003.
[17] M. Elboujdaini, R.W. Revie, Metallurgical factors in stress-corrosion cracking (SCC) and hydrogen-induced cracking (HIC), J. Solid State Electrochem. 13 (2009) 1091–1099.
[18] Yong Hua, Sikiru Mohammed, Richard Barker, Anne Neville, Comparisons of corrosion behaviour for X65 and low Cr steels in high pressure CO2-saturated brine, J. Mater. Sci. Technol. 41 (2020) 21–32, https://doi.org/10.1016/j.jmst.2019.08.050.
[19] K. Hulka, J.M. Gray, High temperature processing of line-pipe steels, Proceedings of the International Symposium Niobium 2001, Orlando, Florida, USA, 2001.
[20] M.J. Kim, S.H. Lee, J.G. Kim, J.B. Yoon, Effect of phosphorus on the corrosion behavior of carbon steel in sulfuric acid, Corros. Sci. 66 (2010) 1–9.
[21] K. Jüttner, Electrochemical impedance spectroscopy (EIS) of corrosion processes on inhomogeneous surfaces, Electrochim. Acta 35 (10) (1990) 1501–1508, https://doi.org/10.1016/0013-4686(90)80004-8.
[22] C. Liu, C. Li, Z. Che, et al., Influence of cementite coarsening on the corrosion resistance of high strength low alloy steel, npj Mater. Degrad. 7 (2023) 43, https://doi.org/10.1038/s41529-023-00358-1.
[23] Zhihui Wang, Xian Zhang, Lin Cheng, Jing Liu, Kaiming Wu, Role of inclusion and microstructure on corrosion initiation and propagation of weathering steels in marine environment, J. Mater. Res. Technol. 10 (2021) 306–321, https://doi.org/10.1016/j.jmrt.2020.11.096.
[24] R.J. Biernat, R.G. Robins, High-temperature iron-water potential/pH diagrams and iron-water-sulfur systems, Electrochim. Acta 17 (1972) 1261–1283.
[25] D.M. Dražic, V. Vaščić, The inflection point in the polarization curve and its use in corrosion rate measurement, Corros. Sci. 25 (1985) 483–491.
[26] P.R. Roberge, Handbook of Corrosion Engineering, McGraw-Hill, New York, USA, 2000.
[27] R.W. Revie, H.H. Uhlig. Corrosion and Corrosion Control, Third ed., John Wiley and Sons, New York, USA, 2008.
[28] WOLYNEC, Stephan. Técnicas eletroquímicas em corrosão. São Paulo: EDUSP. 2003.
[29] M.A. Veloz, I. González, Electrochemical study of carbon steel corrosion in buffered acetic acid solutions with chlorides and H2S, Electrochim. Acta 48 (2002) 135–144.
[30] Frederick Pessu, Richard Barker, Fakuen Chang, Tao Chen, Anne Neville, Iron sulphide formation and interaction with corrosion inhibitor in H2S-containing environments, J. Pet. Sci. Eng. 207 (2021), https://doi.org/10.1016/j.petrol.2021.109152.